

Imperial College London. The wire array loads consisted of eight 18 μm diameter tungsten wires, 20 mm long, distributed evenly about a 16 mm diameter. Measurements were taken 120 ns after current start.

The TS diagnostic [22,23] was used to measure the ion feature of the collective TS spectrum, which is sensitive to the flow velocity and temperature of the plasma. For these experiments the scattering geometry was modified from that employed previously [see Figure 1(b) and 1(c) for diagrams]. The TS probe beam (8 ns, 3 J, 532 nm) propagates in the r - z plane, crossing the axis at the center of the array, at an angle 22.5° from the axis; TS measurements are taken in the same plane, at $\theta = 45^\circ$ and 135° either side of the probing beam. This geometry allows separate measurements of the radial (v_r) and axial (v_z) components of the ion flow velocity [note that the axial and radial scattering vectors, $|k_s| = 2|k_i| \sin(\theta/2)$, have different magnitudes in this geometry ($|k_{sz}|/|k_{sr}| = 2.4$), and thus different TS Doppler shift sensitivities $\delta\omega_D = \vec{k}_s \cdot \vec{v}$].

Scattered light is collected from seven discrete scattering volumes, evenly spaced across 3.3 mm of the array diameter, and imaged onto a pair of linear fiber-optic arrays positioned at the two collection angles. The fiber-optic arrays each consist of 7 fibers (200 μm fiber diameter, 390 μm separation, 2.34 mm overall length); the light they collect is coupled to a time gated ANDOR imaging spectrometer (0.5 m, 2400 line/mm, $\delta\lambda = 0.5 \text{ \AA}$). Alignment is performed under vacuum prior to the experiment by scattering the probe beam off a movable metal pin (100 μm), guaranteeing that the two fiber arrays collect TS signals from the same plasma volumes. Simultaneous end-on laser interferometry [15,24] [500 ps, 500 mJ, 355 nm, e.g., Figure 1(a)] produces axially averaged $r - \theta$ electron density (n_e) maps of the plasma.

Figure 2(a) shows the raw TS spectrogram; the vertical and horizontal axes correspond, respectively, to the distance along the spectrometer input slit and the direction of spectral dispersion. The 14 horizontal bands correspond to the individual spectra collected by each fiber, the top seven

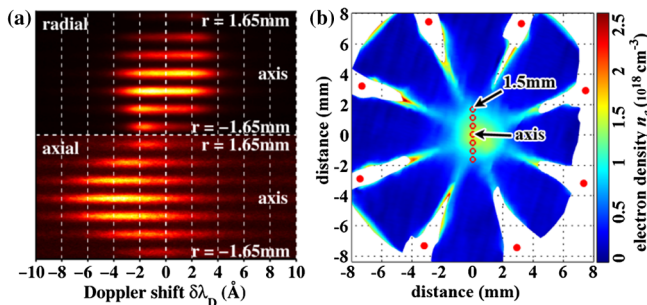


FIG. 2 (color online). (a) Raw Thomson scattering spectrogram. (b) Electron density map extracted from simultaneous end-on interferometry data (355 nm). Red rings show scattering volumes.

to the fibers sensitive to v_r (45° scattering), the bottom seven to the fibers sensitive to v_z (135° scattering). Figure 2(b) shows the n_e distribution, extracted from an end-on interferogram captured simultaneous to the TS measurement, showing the azimuthally smooth “interaction region” [15] extending out to $r \sim 1.5 \text{ mm}$. The seven radial positions from which the TS spectra were collected are marked on this plot by red rings (the initial wire positions are marked by filled red dots). The outermost collection volumes are at $r = 1.65 \text{ mm}$ either side of the array axis, such that the TS measurements cover the entire interaction region. Figure 3(a) contains profiles extracted from the raw TS data (black, solid lines). These were calculated by summing the pixel intensities across the spatial width of each fiber and subtracting any background continuum self-emission (dotted blue lines show the unshifted probe calibration spectrum).

Qualitative inspection of the radial TS spectra reveals direct evidence of flow interpenetration. Each of the spectra [Figure 3(a)] appears to consist of two superimposed TS peaks. The outermost spectra (at $r = \pm 1.65 \text{ mm}$) are almost mirror images of one another; each consists of a narrow-width ($\Delta\lambda$), strongly Doppler-shifted ($\delta\lambda_D$) peak superimposed over a broad, relatively unshifted distribution. The narrow peaks correspond to incoming ablation flows; these flows have large bulk radial velocity v_r and relatively low T_i leading to the large $\delta\lambda_D$ and small $\Delta\lambda$, respectively. The broad, unshifted distributions correspond to scattering from flows that have already passed through

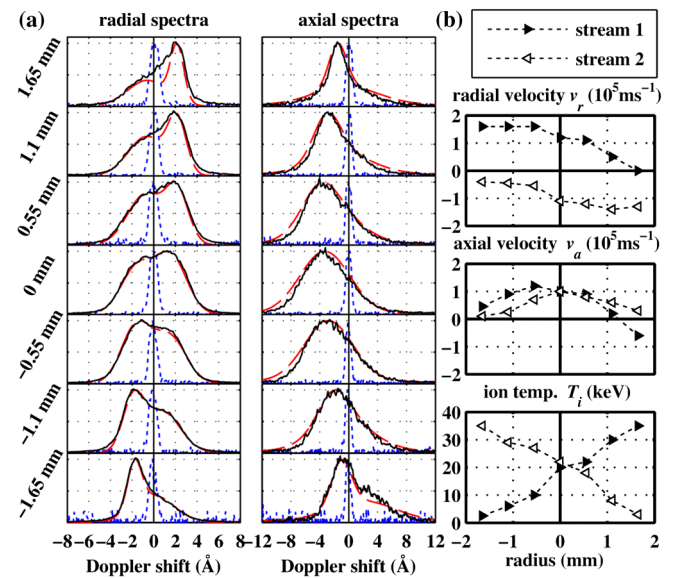


FIG. 3 (color online). (a) Black solid lines show TS profiles extracted from Figure 2(b), red dashed lines show fits, blue dotted lines show the unshifted probe beam spectrum. (b) Radial dependence of v_r , v_z , and T_i used to calculate the fits plotted in (a). The direction of the arrow heads indicates the direction of radial propagation of each stream.

the axis. These flows have partially stagnated, which accounts for their smaller $|\delta\lambda_D|$ and larger $\Delta\lambda$. Scanning through the spectra from other radial positions reveals a continuous evolution of the TS spectrum. As they approach the axis, the $|\delta\lambda_D|$ of the two peaks decreases, and $\Delta\lambda$ increases, which corresponds to decreasing v_r and increasing T_i . On axis the radial spectrum is approximately symmetric; the two peaks have the same $\Delta\lambda$ and equal but opposite $\delta\lambda_D$. These trends indicate that although the flows interpenetrate, they are not fully collisionless; the flows appear to stagnate over a range equal to the diameter of the interaction region, ~ 3 mm.

Inspection of the axial spectra reveals that the ablation flows acquire significant axial velocity v_z as they approach the array axis. As far as we are aware, this phenomenon has never before been observed in any wire array z -pinch experiment. The spectra from the outermost fibers are centered near $\delta\lambda_D \sim 0$, corresponding to a very small net v_z ; this is as expected, since the force geometry in a z -pinch configuration should lead to mostly radial ablation flows. Closer to the array axis, however, the centers of the spectral peaks shift strongly towards negative $\delta\lambda_D$. This shift, which peaks on axis, corresponds to an increasing v_z towards the anode. This measurement of radially increasing v_z is highly reproducible. Given the direction of this axial velocity (opposite to applied electric field), it seems likely that the origin of the effect is magnetic (discussed in detail later).

The $\Delta\lambda$ of the axial spectra behave in a similar manner to those of the radial spectra, providing strong evidence that the observed broadening is due to an isotropic increase in the T_i of the plasma, and not simply to the superposition of many plasma streams in the r - θ plane (i.e., an effective temperature). In Figure 3(a) the axial spectra are broader than the radial spectra, but this is in fact due to the difference in magnitude between the two scattering vectors; the $\Delta\lambda$ of the two spectra actually correspond to the same values of T_i .

The measured spectral profiles were fitted using the equations for the nonrelativistic, Maxwellian TS form factor [25], $S(k, \omega)$:

$$S(k, \omega) = \frac{2\pi}{k} \left| 1 - \frac{\chi_e}{\epsilon} \right|^2 f_{eo} \left(\frac{\omega}{k} \right) + \sum_j \frac{2\pi \bar{Z}_j^2 n_j}{k n_i} \left| \frac{\chi_e}{\epsilon} \right|^2 f_{jo} \left(\frac{\omega}{k} \right),$$

$$\epsilon = 1 + \chi_e + \sum_j \chi_j, \quad n_i = \sum_j n_j.$$

This equation sums the effects of the electrons and multiple ion populations (labeled j), each of which may have a separate velocity and temperature; f_{eo} and f_{jo} are the Maxwellian velocity distribution functions and χ_e and χ_j are the susceptibilities for the electron and ions, respectively, ϵ is the total permittivity of the plasma, n_j and \bar{Z}_j are the density and average ionization of each ion population, and n_i is the total ion density. The plasma was

modeled as consisting of two counterpropagating ion populations (henceforth “streams”) ($j = 1, 2$), each described by a set of independent parameters, n_j , T_j , v_{rj} , and v_{zj} . Since the electron thermal velocity is much larger than the plasma flow velocity, the electrons were treated as a single fluid with a single temperature T_e , and the two streams were assigned the same \bar{Z}_j based on the assumption that ionization processes are dominated by electron-ion collisions. Variations in T_e and \bar{Z} within reasonable ranges had little effect on the ion feature. The values of these parameters were therefore set at $T_e = 20$ eV and $\bar{Z} = 6$, based on previous estimates [15]. The electron density n_e , measured via interferometry [Figure 2(a)], was used to constrain $n_i \bar{Z}$. For each scattering volume, the radial and axial spectral profiles were calculated and fitted simultaneously, the only difference between the two calculations being the flow velocity components (v_{rj} or v_{zj}) and scattering vectors (k_{sr} or k_{sz}) used. The plasma parameters were varied in order to produce the best fit to each pair of measured TS spectra; the results are plotted as red dashed lines in Figure 3(a). The fits match the data well, especially given the constraints applied to the model used to calculate them.

Figure 3(b) shows plots of the radial dependence of the dominant fitting parameters for each stream. Radii to the left of the axis are denoted negative in these plots in order to simplify discussion. Errors in the determination of the plasma parameters were estimated by assessing the range over which an acceptable fit could be produced. The errors in the determination of v_r and v_z were $\pm 1 \times 10^4$ and $\pm 5 \times 10^3$ ms^{-1} , respectively (axial scattering has greater sensitivity). Errors in the determination of T_i were $\pm T_i/6$. The error ranges do not significantly impact the overall trends shown in Figure 3(b). As might be expected, the behavior of the streams is very symmetric. The following discussion focuses on the right propagating stream (black triangles); however, it is equally valid for the left propagating stream. At $r = -1.65$ mm, the stream is approaching the axis with $v_r \sim 1.6 \times 10^5$ ms^{-1} , $v_z \sim 0.2 \times 10^5$ ms^{-1} and an effective T_i of ~ 2 – 3 keV. At the axis, v_r decreases to $\sim 1.2 \times 10^5$ ms^{-1} , while v_z and T_i increase to $\sim 1 \times 10^5$ ms^{-1} and ~ 20 keV, respectively. At this point the ions have almost equal radial and axial velocity. On the far side of the axis, v_r and v_z both steadily decrease, becoming negligible at $r = 1.65$ mm; the T_i of the fully stagnated stream is ~ 35 keV.

Although the values for T_i quoted above appear very large, they are on the order of the incoming kinetic energy per ion [$\text{KE} = m_i(v_r^2 + v_z^2)/2$]. At $r = -1.65$ mm, KE is ~ 25 keV, and the total energy per ion ($E_T = \text{KE} + 3k_B T_i/2$) is ~ 28 keV, while on axis E_T is a bit larger, KE ~ 23 keV and $E_T \sim 23 + (3/2 \times 20) = 53$ keV. The difference in E_T may be explained by a time variation in the launch velocity of the flow. The time of flight from the edge of the interaction region to the axis is 15 ns ($r = 1.65$ mm,

$v_r = 1 \times 10^5 \text{ ms}^{-1}$). TS measurements taken simultaneously over a range of radii therefore actually correspond to a range of flow launch times. The E_T observed on axis, 53 keV, implies an initial $v_r \sim 2.4 \times 10^5 \text{ ms}^{-1}$, assuming no energy loss to ionization or radiation. The large T_i values measured in this experiment are consistent with the defocusing of the ablation streams and formation of the azimuthally smoothed region observed near the array axis [15]; at $T_i = 20 \text{ keV}$ the ion thermal velocity on axis $v_{\text{Th}} \sim 1 \times 10^5 \text{ ms}^{-1}$ is comparable to both v_r and v_z , and should drive significant divergence of the stream. The ion-ion mean free path required to explain the observed heating is $\sim 3 \text{ mm}$.

The large T_i values measured imply that the ions are unable to cool. Efficient ion cooling requires rapid transfer of ion thermal energy to the electrons. For the parameters discussed above the ion-electron equilibration time τ_e^{i-e} [26] is $\sim 50 \text{ ns}$. At $v_r \sim 1 \times 10^5 \text{ ms}^{-1}$ the ions would travel 5.5 mm over this time scale, further than the 3 mm diameter of the interaction region; equilibration is therefore quite slow. Earlier in time, when the density of the plasma is lower, τ_e^{i-e} will be even larger, leading to even slower equilibration. This is consistent with previous measurements of the formation dynamics of dense precursors, which appear later in the ablation phase of wire arrays z pinches. These are thought to be formed by the rapid, nonlinear, radiative collapse of the earlier broad axial distribution of plasma [16,17] triggered by the onset of rapid ion-electron equilibration. For the experimental setup used in these experiments, precursor collapse occurs $\sim 30\text{--}50 \text{ ns}$ after the time of measurement.

The most likely explanation for the observed magnitude and direction of the v_z on axis is that it is the result of the deflection of the ion trajectories by a static magnetic field accumulated in the interaction region. This explanation is not only consistent with the otherwise counterintuitive anodewise direction of v_z , but also with the decrease in v_z seen after each stream has passed through the axis (as the direction of the $\vec{v} \times \vec{B}$ force should reverse). The magnetic Reynolds number, $\text{Re}_m = Lv/\eta$, describes the relative importance of magnetic advection and diffusion in dynamic structures; the magnetic diffusion of interest is perpendicular to the field, so the magnetic diffusivity η is calculated using the transverse Spitzer resistivity [27], $\eta = 81.9\lambda_C \bar{Z} T_e^{-3/2} [\text{m}^2 \text{ s}^{-1}]$ (T_e in eV). Using a Coulomb logarithm of $\lambda_c \sim 6$ [28], $\bar{Z} = 6$ and $T_e = 20 \text{ eV}$ results in $\eta \sim 35 \text{ m}^2 \text{ s}^{-1}$. Taking the system scale size L as the scale length of the ablation flows (i.e., the array radius), 8 mm, and the scale velocity v as the flow velocity seen on axis, $1 \times 10^5 \text{ ms}^{-1}$, leads to $\text{Re}_m \sim 23$, indicating that the ablation streams are advecting the global magnetic field to the axis, consistent with previously reported observations [19,20]. The large Re_m also implies that the field embedded in the radially converging flows should stagnate on the axis. The direction of this stagnated field would

produce a $\vec{v} \times \vec{B}$ force which would steer incoming ions towards the anode and outgoing ions towards the cathode, matching our observations. The magnetic diffusion time, $\tau_{\text{DM}} = L^2/\eta$, describes the typical time scale for resistive diffusion of the magnetic field across length scale L . Setting $L \sim 1 \text{ mm}$ gives $\tau_{\text{DM}} \sim 30 \text{ ns}$, the time scale for the diffusion and dissipation of the magnetic field over the radius of the interaction region. This period is long enough to allow the buildup of an enhanced static magnetic field in the vicinity of the axis (note that η was calculated using $T_e = 20 \text{ eV}$; T_e on axis may be higher, leading to even larger τ_{DM}).

On axis, the measured ion velocity components indicate that the ion flows are deflected by $\sim 45^\circ$. This degree of deflection would be expected to occur over a distance $\sim r_i/\sqrt{2}$, where r_i is the ion gyroradius. Equating this distance to the interaction region radius ($r = 1.65 \text{ mm}$) and rearranging produces an estimate for $\bar{Z}B$ of $\sim 130 \text{ T}$. Our previous estimate of $\bar{Z} = 6$ then suggests a toroidal magnetic field of $\sim 22 \text{ T}$. The presence of a toroidal magnetic field about the axis implies there must be current flowing on axis; the net current required to produce 20 T at $r = 1 \text{ mm}$ is $I = 2\pi r B/\mu_0 \sim 100 \text{ kA}$. If the field is this strong, it may be possible to measure its structure directly using optical Faraday rotation techniques currently under development.

The data and analysis presented in this Letter represent the first direct measurements of the collision, interpenetration, and stagnation of cylindrically convergent, high Mach number, magnetized plasma flows. A \bar{Z} of ~ 12 is required in order to reproduce the observed $\sim 3 \text{ mm}$ stagnation length using the classical mean free path [26]; this is larger than previously estimated [15]. Direct measurements of \bar{Z} are needed to assess the importance of anomalous scattering; however, the two stream and Weibel instabilities are unlikely to be important as both saturate for $T_i \gg 0.27\bar{Z}T_e$ [29]. The strength of the inferred magnetic field is sufficient only to deflect the ions, not fully magnetize them, suggesting that magnetized instabilities are also unlikely to be important.

The measurements also show a deflection of the ablation streams towards the anode as they approach the array axis; this is a novel observation, likely caused by a Lorentz $\vec{J} \times \vec{B}$ force acting on the ions due to their interaction with a static magnetic field which builds up about the axis. Further work is required in order to confirm the presence of this magnetic field to and properly understand its formation and structure. The quantitative and detailed nature of these measurements makes them ideally suited for code verification and model validation exercises. It should be noted, however, that the deflection and interpenetration dynamics observed will not be reproduced using the fluid magnetohydrodynamics approaches typically used to model wire array dynamics; particle-in-cell or hybrid techniques will be required in order to properly reproduce the experimental results.

This work was supported in part by EPSRC Grant No. EP/G001324/1, by DOE cooperative agreements No. DE-F03-02NA00057 and No. DE-SC-0001063, and by Sandia National Laboratories.

*Present address: Lawrence Livermore National Laboratory, P.O. Box 808, Livermore, California 94551, USA.

- [1] D. D. Ryutov *et al.*, *Phys. Plasmas* **8**, 1804 (2001).
- [2] O. Rancu *et al.*, *Phys. Rev. Lett.* **75**, 3854 (1995).
- [3] H.-S. Park *et al.*, *High Energy Density Phys.* **8**, 38 (2012).
- [4] J. S. Ross *et al.*, *Phys. Plasmas* **19**, 056501 (2012).
- [5] Y. Kuramitsu *et al.*, *Phys. Rev. Lett.* **106**, 175002 (2011).
- [6] C. Constantin *et al.*, *Astrophys. Space Sci.* **322**, 155 (2009).
- [7] N. L. Kugland *et al.*, *Nat. Phys.* **8**, 809 (2012).
- [8] D. D. Ryutov, N. L. Kugland, M. C. Levy, C. Plechaty, J. S. Ross, and H. S. Park, *Phys. Plasmas* **20**, 032703 (2013).
- [9] D. D. Ryutov, N. L. Kugland, H.-S. Park, S. M. Pollaine, B. A. Remington, and J. S. Ross, *Phys. Plasmas* **18**, 104504 (2011).
- [10] P. M. Nilson *et al.*, *Phys. Plasmas* **15**, 092701 (2008).
- [11] M. Yamada, R. Kulsrud, and H. Ji, *Rev. Mod. Phys.* **82**, 603 (2010).
- [12] D. D. Ryutov, *Astrophys. Space Sci.* **336**, 21 (2011).
- [13] O. V. Gotchev, J. P. Knauer, P. Y. Chang, N. W. Jang, M. J. Shoup, D. D. Meyerhofer, and R. Betti, *Rev. Sci. Instrum.* **80**, 043504 (2009).
- [14] T. Morita *et al.*, *EPJ Web Conf.* **59**, 15004 (2013).
- [15] G. F. Swadling *et al.*, *Phys. Plasmas* **20**, 062706 (2013).
- [16] S. V. Lebedev, F. N. Beg, S. N. Bland, J. P. Chittenden, A. E. Dangor, M. G. Haines, S. A. Pikuz, and T. A. Shelkovenko, *Laser Part. Beams* **19**, 355 (2001).
- [17] S. Bott *et al.*, *Phys. Rev. E* **74**, 046403 (2006).
- [18] D. B. Sinars, M. E. Cuneo, E. P. Yu, S. V. Lebedev, K. R. Cochrane, B. Jones, J. J. MacFarlane, T. A. Mehlhorn, J. L. Porter, and D. F. Wenger, *Phys. Plasmas* **13**, 042704 (2006).
- [19] V. V. Aleksandrov, V. A. Barsuk, E. V. Grabovski, A. N. Gritsuk, G. G. Zukakishvili, S. F. Medovshchikov, K. N. Mitrofanov, G. M. Oleinik, and P. V. Sasorov, *Plasma Phys. Rep.* **35**, 200 (2009).
- [20] J. Greenly *et al.*, *AIP Conf. Proc.* **1088**, 53 (2009).
- [21] I. H. Mitchell, J. M. Bayley, J. P. Chittenden, J. F. Worley, A. E. Dangor, M. G. Haines, and P. Choi, *Rev. Sci. Instrum.* **67**, 1533 (1996).
- [22] A. J. Harvey-Thompson *et al.*, *Phys. Plasmas* **19**, 056303 (2012).
- [23] A. J. Harvey-Thompson *et al.*, *Phys. Rev. Lett.* **108**, 145002 (2012).
- [24] G. F. Swadling *et al.*, *Phys. Plasmas* **20**, 022705 (2013).
- [25] J. Sheffield, D. Froula, S. H. Glenzer, and N. C. Luhmann, Jr., *Plasma Scattering of Electromagnetic Radiation: Theory and Measurement Techniques* (Academic Press, New York, 2010), p. 104.
- [26] B. A. B. Trubnikov, *Reviews of Plasma Physics*, Vol. 1 (Consultants Bureau, New York, 1965), p. 126–137.
- [27] L. Spitzer, *Physics of Fully Ionized Gases* (Courier Dover Publications, Mineola, New York, 2013), p. 136.
- [28] D. Book and J. D. Huba, *NRL Plasma Physics Formulary* (NRL, Washington DC, 2002).
- [29] R. L. Berger, J. R. Albritton, C. J. Randall, E. A. Williams, W. L. Kruer, A. B. Langdon, and C. J. Hanna, *Phys. Fluids B* **3**, 3 (1991).